CT NUMBERS INFERRED FROM CONE-BEAM COMPUTED TOMOGRAPHY

O.-T. DAVID[*], *OANA MUNTEANU*[*], *R.-A. TUCE*[*], *A. NEAGU*[*,**,#], *F. BÎRSĂŞTEANU*[***]

[*]Center for Modeling Biological Systems and Data Analysis, "Victor Babeş" University of Medicine and Pharmacy, Timişoara, Romania, [#]e-mail: neagu@umft.ro
[**]Department of Physics and Astronomy, University of Missouri, Columbia, U.S.A.
[***]Discipline of Radiology and Medical Imaging, "Victor Babeş" University of Medicine and Pharmacy, Timişoara, Romania

Abstract. Preoperative assessment of bone quality in the dental arches is important in implantology. Fan-beam computed tomography (CT) proved to be successful in this respect, although it involves high costs and excessive radiation exposure. Bone density estimated by CT correlates well with the mechanical bone density scale proposed by Misch [14]. Ranges of CT numbers, expressed in Hounsfield units (HU), were associated to various bone density classes. About an order of magnitude cheaper and less harmful than CT, cone-beam computed tomography (CBCT) has attracted much attention as an alternative technique for bone quality estimation. CBCT voxel values, however, are less informative than CT numbers because they depend on position, on instrument settings and type. This paper proposes a mathematical procedure for making corrections to CBCT voxel values in order to eliminate their position-dependence and to bring them closer to CT numbers. An anthropomorphic spine phantom, as well as granular $CaCl_2$ and bone meal were scanned using both CT and CBCT. We found a mathematical relationship between CT numbers and CBCT voxel values, and used nonlinear least squares methods to find the model parameters that provided the best fit to experimental data. We validated our procedure for a few materials and one type of CBCT unit. Further research will be needed to test the feasibility of this procedure for other types of CBCT instruments. The approach proposed here might become clinically useful if model parameters will be identified for hard tissues from the oral environment.

Key words: CBCT voxel values, bone quality, implantology.

INTRODUCTION

The stability of a dental implant depends on the quality of the alveolar bone at the insertion site. Bone quality is important not only for the early-stage stability of the implant, but also for its long-term survival [7]. To characterize the bone from dental arches, Misch proposed a qualitative bone density scale that is based on the

Received: May 2017;
in final form May 2017.

ROMANIAN J. BIOPHYS., Vol. 27, Nos 1–2, P. 1–12, BUCHAREST, 2017

torque needed to insert the implant [13]: D1 bone is dense cortical bone, D2 bone is coarse trabecular bone covered by a thick layer of dense to porous cortical bone on the crest, D3 bone is fine trabecular bone covered by a thin layer of porous cortical bone on the crest, D4 bone is fine trabecular bone, whereas D5 bone is insufficiently mineralized, immature bone.

Mechanical assessment of bone quality can only be done intraoperatively, by highly qualified implantologists. Therefore, much research has been devoted to the preoperative evaluation of bone quality by medical imaging. Fan-beam computed tomography (CT) was found useful in characterizing bone density in terms of CT numbers (radiodensity) expressed in Hounsfield units (HU) [5, 8, 9, 11, 14, 17, 22, 23]: the radiodensity of D1 bone is larger than 1,250 HU, that of D2 bone ranges between 850 HU and 1,250 HU, that of D3 bone lies in the interval 350 HU to 850 HU, that of D4 bone ranges from 150 HU to 350 HU, while D5 bone is characterized by CT numbers below 150 HU.

Fan-beam CT imaging, however, exposes the patient to a relatively high dose of ionizing radiations, of the order of 1 mSv (1.3–3.3 mSv for the mandible and 1.0–1.4 mSv for the maxilla) [21]. A better option for the 3D imaging of hard tissues of the head and neck is cone-beam computed tomography (CBCT) [6]. The architecture of CBCT instruments was inspired by panoramic X-ray units. A CBCT unit exposes the patient to a relatively small radiation dose by collimating the X-ray beam to the area of interest and by recording snapshots on a flat-panel detector [12]. The effective dose received by the patient, during a CBCT recording, is of the order of 10–100 μSv [21]. As a result of the progress in digital flat-panel detector technology, CBCT units became an order of magnitude cheaper than multislice CT scanners. Moreover, a CBCT device provides remarkable image accuracy, with isotropic (cube shaped) voxels of 0.2 mm side length. The voxels of a spiral CT are anisotropic, with the longest side of the order of 1 mm [21]. On the other hand, the contrast resolution of a CBCT instrument is about an order of magnitude smaller than that of a fan-beam CT scanner, mainly due to X-ray scatter generated in the exposed volume [12].

The use of CBCT voxel values for characterizing bone quality is appealing because a CBCT acquisition is less expensive and involves less radiation exposure than CT. CBCT image analysis programs include tools that provide descriptive statistics of HU values of voxels enclosed in a selected region. As a result of CBCT studies [4, 10], a scale of voxel values has been established in reasonable agreement with CT and with the known hierarchy of bone densities encountered in various regions of the jaws. Nevertheless, CBCT voxel values were deemed unreliable because they depend on device, imaging parameters, and positioning [15, 19]. The use of CBCT for bone quality assessments is intensely debated in the literature [1, 2, 3, 20].

The aim of this paper is to improve the reliability of bone quality estimation by CBCT. Based on a comparative analysis of CT scans and CBCT acquisitions of the same phantom, we propose a mathematical procedure for converting CBCT voxel values into CT numbers. More precisely, our procedure provides corrections to CBCT voxel values, rendering them less sensitive to location and closer to CT numbers obtained from fan-beam CT imaging. In this work, we validate our procedure for a few materials and a single type of CBCT instrument, ProMax 3D (Planmeca, Finland).

MATERIALS AND METHODS

We analyzed CT and CBCT recordings of bone meal (Trixie Heimtierbedarf GmbH & Co., Germany), granular $CaCl_2$ (Chimcomplex Borzeşti, România), and an anthropomorphic spine phantom model DPA/QDR-1 (Hologic Inc., MA, USA) produced for the calibration of dual energy X-ray absorptiometry (DXA) bone density scanners.

CT acquisitions were done using a LightSpeed Ultra spiral CT scanner (GE Medical Systems, USA) at 120 kV X-ray tube voltage and 100 mA current intensity. CBCT scans were done using a ProMax 3D CBCT instrument (Planmeca, Finland) at 90 kV voltage and a set of X-ray tube currents (10 mA, 12 mA and 14 mA); for each current intensity, the CBCT device was used in three different radiation dose settings: low dose (ld), normal dose (nd), and high dose (hd).

Bone meal powder and granular $CaCl_2$ were placed in cylindrical plastic containers of 10 cm diameter and 10 cm height. The CT recording was done for the whole sample, whereas the CBCT recording was done for a cylindrical field of view (FOV) of 8 cm diameter and 8 cm height whose axis of symmetry coincided with that of the plastic container.

The DXA calibration phantom was scanned entirely by CT, and partially by CBCT, with a cylindrical field of view (FOV) of 8 cm in diameter and height, centered on a region of low radiodensity (Fig. 1, dashed circle).

Both CT and CBCT recordings were visualized and analyzed with the Romexis 3.0.1.R software (Planmeca, Finland). Using the Measure Ellipsoid tool, a spherical region of 9 mm in diameter was selected (circle surrounded by four squares in Fig. 1), and the tool reported the descriptive statistics of the HU values of the enclosed voxels (white text on Fig. 1). The first line of the report gives the volume of the selected region in cm^3, the second lists the size of the region (width, height, and depth), the third gives the mean of the HU values of the voxels that compose the selected region, the fourth gives the standard deviation of these HU values, and the fifth specifies the range of HU values encountered in the region.

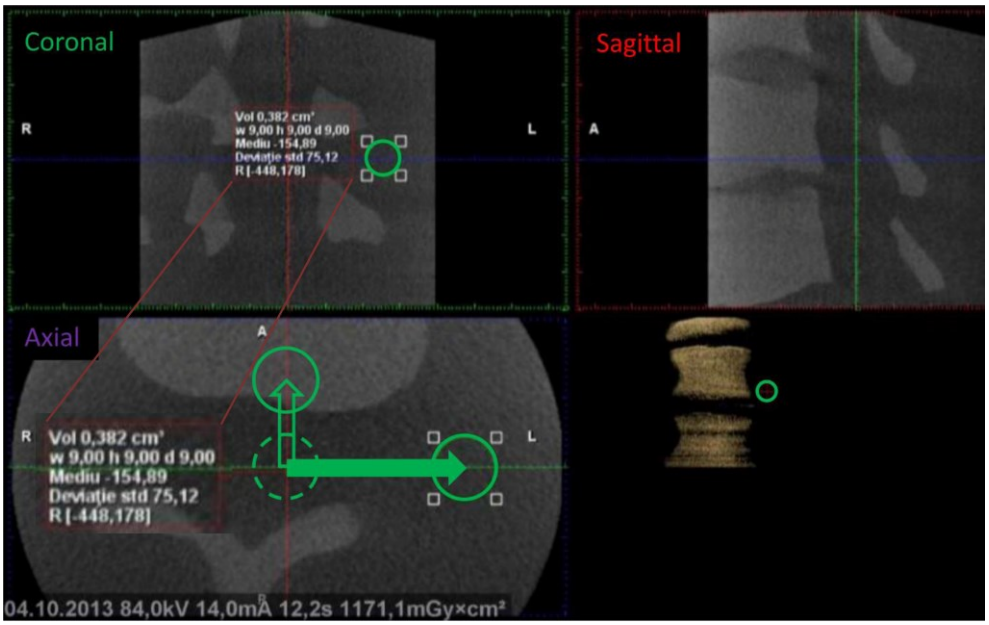

Fig. 1. CBCT recording of a human spine phantom used for calibrating DXA scanners. The field of view (FOV) was a cylinder of 8 cm diameter and 8 cm height. Mean voxel values were obtained using the Measure Ellipsoid function from Romexis. The output of one measurement (text written in white type, magnified for clarity in the axial view) is the descriptive statistics of HU values of the voxels that compose the region of interest – a sphere of 9 mm in diameter. It specifies the volume of the region of interest (Vol), its width (w), height (h) and depth (d), the mean of the voxel values (Mediu), their standard deviation (Deviatie std), and their range (R).

We first analyzed voxel values in a sphere whose center lied on the symmetry axis of the FOV (dashed circle on Fig. 1). Then we moved the selected sphere by 1 mm along a horizontal direction, repeated the analysis, and continued this procedure along a distance of 34 mm. In the phantom, we analyzed a homogeneous region (Fig. 1, solid arrow) as well as an inhomogeneous one (Fig. 1, empty arrow, postero-anterior direction).

To describe the mathematical relationship between CT numbers and CBCT voxel values, we proposed an empirical formula. The corresponding model parameters were obtained by fitting experimental data with a nonlinear least-squares procedure written in MATLAB 7.13 (The MathWorks, Natick, MA, USA).

RESULTS

To obtain radiodensity estimates based on a CT as well as CBCT recording, we scanned a bone density phantom using a CT scanner at 120 kV accelerating voltage and 100 mA X-ray tube current at a slice thickness of 0.313 mm. Then we

scanned the same phantom using a CBCT instrument at a 90 kV accelerating voltage and three different X-ray tube currents (10, 12, and 14 mA). Moreover, for each voltage-current combination we tested three different radiation dose settings: low dose (ld), normal dose (nd), and high dose (hd).

We analyzed each of these scans to infer the average HU values of the voxels contained in a set of spherical domains of 9 mm in diameter, centered on a coordinate axis 1 mm apart (Fig. 1, solid arrow). The results of these 10 analyses are depicted in Fig. 2. Here stars represent average CT numbers *vs.* position for a roughly homogeneous portion of the phantom (Fig. 1, solid arrow). These CT numbers were obtained by analyzing the CT recording with the help of the Measure Ellipsoid tool from Romexis. In Fig. 2, squares, circles, and diamonds represent HU values returned by the Measure Ellipsoid tool when CBCT recordings were analyzed. As explained in the figure legend, small squares depict CBCT voxel values obtained when the 90 kV, 10 mA, low-dose recording was analyzed (CBCT90x10ld), empty squares refer to 90 kV, 12 mA, low-dose recording and so on.

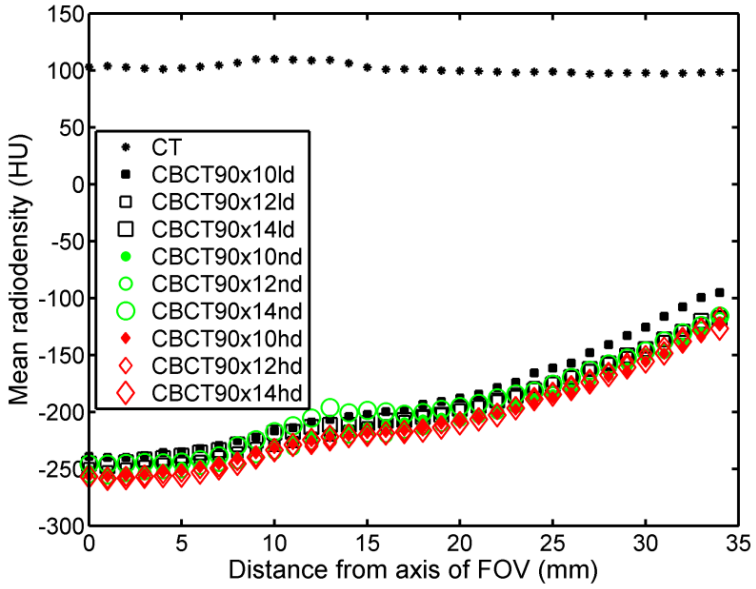

Fig. 2. Average HU values of voxels contained in a set of 35 spheres whose centers are located 1 mm apart along an axis that is perpendicular to the symmetry axis of the field of view (FOV) and traverses a homogeneous portion of the phantom (Fig. 1, solid arrow). Different markers refer to different recordings of the same phantom: stars depict CT data, whereas squares, circles and diamonds depict CBCT data for different settings of the instrument. For example, large, empty diamonds represent radiodensity *vs.* distance for the CBCT acquisition obtained at 90 kV voltage, 14 mA filament current intensity, and high-dose (hd) regime.

While the analysis of adjacent regions that include thousands of voxels leads to a smooth function of position, the question arises whether the average HU data depend on the shape and size of the selected region. Figure 3 addresses this question by depicting average HU values of the set of pixels contained in spheres of 9 mm in diameter (represented as stars for CT and solid disks for CBCT), spheres of 5 mm in diameter (represented as crosses for CT and empty circles for CBCT), and squares of 5 mm side length (represented as + signs for CT and squares for CBCT).

Figures 2 and 3 indicate that CT numbers are the same for all portions of a homogeneous material, whereas CBCT voxel values depend on the distance, r, between the symmetry axis of the FOV and the center of the analyzed region. Indeed, Fig. 4 indicates that the ratio $(CT+1000)/(CBCT+1000)$ can be fitted with the empirical function

$$f(r)=\frac{a}{1+\left(r/r_0\right)^2}, \tag{1}$$

where a and r_0 are model parameters. In Fig. 4, markers depict the ratio $(CT+1000)/(CBCT+1000)$, while solid lines plot the fit function of Eq. (1), for model parameters given by a nonlinear least-squares fit algorithm. Here CT denotes CT number (radiodensity), expressed in Hounsfield units (HU); CBCT, on the other hand, stands for the voxel values returned by the CBCT image analysis software, Romexis 3.0.1.R.

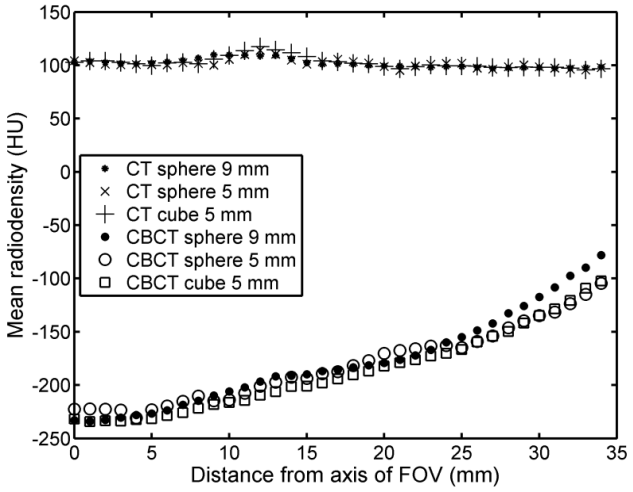

Fig. 3. Average HU values obtained for adjacent regions of different size and shape: large and small spheres (of 9 mm and 5 mm in diameter), and squares (of 5 mm side length).
CBCT data were obtained at 84 kV accelerating voltage and 14 mA filament current intensity.

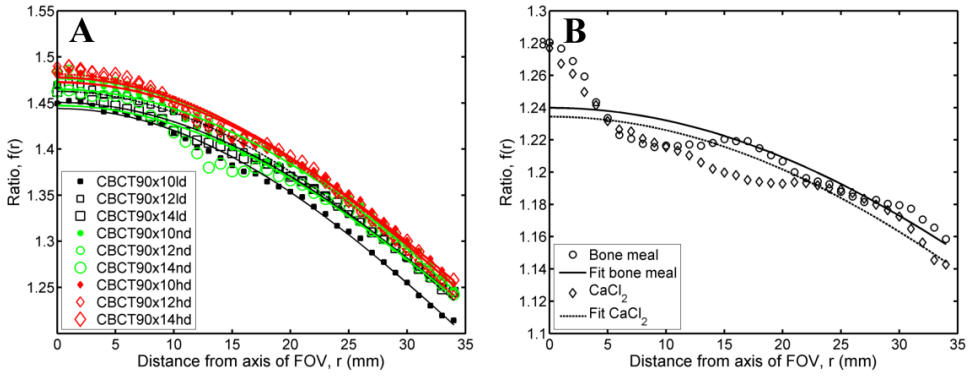

Fig. 4. Nonlinear least squares fit of the ratio $(CT+1000)/(CBCT+1000)$ using the empirical fit function of Eq. (1). A homogeneous portion of the phantom (Fig. 1, solid arrow) was analyzed for various settings of the CBCT scanner (A), along with samples of bone meal and granular $CaCl_2$ (B). CBCT settings are explained in the caption of Fig. 1.

Table 1 lists the model parameters obtained during the nonlinear least squares fit procedure that gave the theoretical curves of Fig. 4.

Table 1

Model parameters obtained by using Eq. (1) to fit the experimental data of Fig. 4. Lines 1 to 9 refer to the homogeneous portion of the DXA phantom (Fig. 1, solid arrow), whereas lines 10 and 11 refer to bone meal powder and granular $CaCl_2$, respectively

No.	**Data set**	a	r_0 **(mm)**	***RMSE***	***R*-square**
1	CBCT90x10ld	1.444 (1.442, 1.447)	77.19 (76.26, 78.12)	0.0047	0.9962
2	CBCT90x12ld	1.463 (1.460, 1.465)	79.40 (78.31, 80.48)	0.0051	0.9950
3	CBCT90x14ld	1.451 (1.447, 1.454)	82.62 (81.20, 84.03)	0.0060	0.9921
4	CBCT90x10nd	1.465 (1.460, 1.469)	82.72 (80.71, 84.73)	0.0086	0.9843
5	CBCT90x12nd	1.476 (1.474, 1.479)	79.32 (78.35, 80.29)	0.0047	0.9960
6	CBCT90x14nd	1.447 (1.440, 1.454)	83.08 (80.00, 86.17)	0.0129	0.9638
7	CBCT90x10hd	1.473 (1.469, 1.476)	82.16 (80.56, 83.76)	0.0070	0.9899
8	CBCT90x12hd	1.481 (1.479, 1.484)	77.36 (76.45, 78.27)	0.0047	0.9963
9	CBCT90x14hd	1.478 (1.474, 1.482)	80.09 (78.50, 81.69)	0.0075	0.9895
10	Bone meal	1.240 (1.233, 1.247)	125.6 (113.6, 137.6)	0.0140	0.7864
11	$CaCl_2$	1.234 (1.227, 1.242)	121.1 (110.2, 132.0)	0.0141	0.8056

The quality of the fit is characterized by the root mean square error (*RMSE*) and by the R-square value (Table 1, last two columns). *RMSE* is a positive number, defined as the square root of the ratio of the sum of squares due to error and the number of degrees of freedom, 33, equal to the number of experimental points minus the number of model parameters. The closer is *RMSE* to zero, the more useful is the fit for prediction. *R*-square is the square of the multiple correlation

coefficient and is defined as a ratio: the sum of squares of the regression divided by the total sum of squares. *R*-square ranges between 0 and 1; the closer is *R*-square to 1, the better is the fit (*i.e.* the greater is the amount of variance described by the model).

Using the model parameters given in Table 1, obtained by nonlinear least squares fits of *CBCT* data, Eq. (1) enables one to calculate *CT* numbers on the basis of *CBCT* measurements. The corrected *CBCT* voxel values, given by the formula

$$CBCT_{\text{corrected}} = -1000 + \frac{a}{1+\left(r/r_0\right)^2}\left(CBCT + 1000\right) \tag{2}$$

are roughly equal to the *CT* numbers extracted from the analysis of a fan-beam CT recording. Therefore, such a procedure results in an improved assessment of the radiodensity of a material in comparison to a CBCT assessment. Nevertheless, when the fit function (Eq. (1)) does not account precisely for the spatial dependence of the *CBCT* voxel values, such as in the case of Fig. 4B, the correction is imprecise, too.

To illustrate the correction of *CBCT* values based on Eq. (2), Fig. 5 plots the average *CT* numbers obtained at various locations in bone meal (stars) and in $CaCl_2$ granules (+ signs). The corresponding *CBCT* voxel values are represented as solid disks and diamonds, respectively. To obtain the corrected *CBCT* voxel values, represented in Fig. 5 as empty circles and diamonds, respectively, we used Eq. (2) with model parameters from Table 1, rows 10 and 11, respectively.

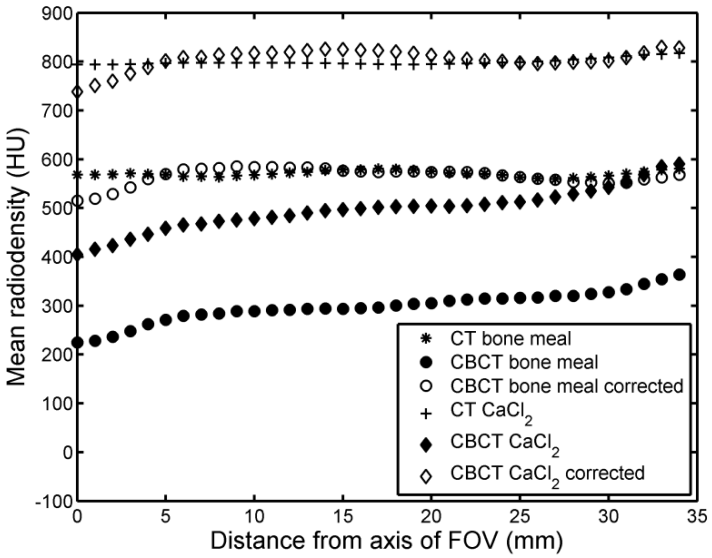

Fig. 5. *CT* numbers and *CBCT* voxel values before correction (solid markers) and after correction (empty markers). Corrected *CBCT* voxel values were given by Eq. (2).

To illustrate the importance of model parameters for an effective correction, Fig. 6 depicts average radiodensities of spherical regions of 9 mm in diameter centered along a postero-anterior axis (Fig. 1, empty arrow). This axis traverses an inhomogeneous region of the DXA calibration phantom. In Fig. 6, stars depict radiodensities evaluated from the CT recording (*CT* numbers); solid disks represent voxel values evaluated from a CBCT recording; empty circles show the corrected *CBCT* voxel values given by Eq. (2), with model parameters inferred from the homogeneous portion of the phantom (Table 1, mean of rows 1–9: a = 1.464 and r_0 = 80.4 mm); empty pentagons show roughly corrected *CBCT* voxel values given by Eq. (2), with model parameters taken as averages of those obtained for bone meal and $CaCl_2$ (Table 1, mean of rows 10 and 11: a = 1.237 and r_0 = = 123.4 mm).

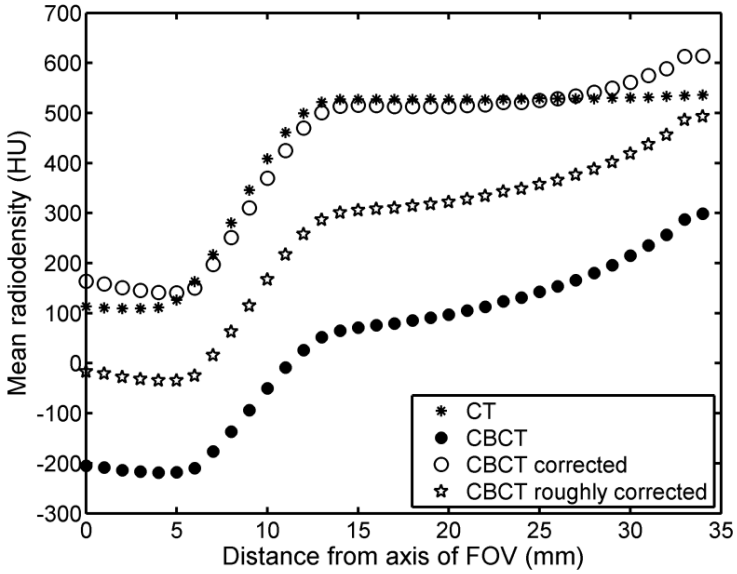

Fig. 6. Corrections of *CBCT* voxel values. The mean radiodensity of voxels enclosed in a set 35 spherical regions of 9 mm in diameter, whose centers are located 1 mm apart along a postero-anterior axis, depicted as an empty arrow in Fig. 1. Star-shaped markers plot radiodensities *vs*. position obtained from a CT recording, solid disks plot *CBCT* voxel values, empty pentagons plot a rough correction of *CBCT* voxel values based on Eq. (2) (the correction is ineffective due to inappropriate model parameters, taken as the average of those obtained for bone meal and $CaCl_2$ granules), whereas circles plot corrected *CBCT* voxel values given by Eq. (2), with model parameters inferred as an average of those obtained for a homogeneous part of the same phantom, at various instrument settings (Table 1, mean values of the parameters listed in lines 1–9).

DISCUSSION

Despite several advantages of CBCT over CT in hard tissue imaging of the head and neck, bone quality estimates based on CBCT imaging are controversial [20]. While most CBCT analysis programs provide tools for assessing voxel values in selected regions, these values are less informative than CT numbers extracted from a fan-beam CT scan. *CBCT* voxel values are expressed in the same units as *CT* numbers (Hounsfield units, HU) and characterize the radiodensity of the visualized tissue sample. Nevertheless, they depend on the location in the FOV as well as on the settings and type of the CBCT instrument [15].

Using two types of CBCT instruments, Oliveira *et al*. [18] scanned a custom-fabricated human skull phantom with various FOVs. Their phantom contained samples of dipotassium hydrogen phosphate solution, of the same concentration, placed in various anatomical locations. The CBCT image analysis software furnished different voxel values for the same solution placed in different locations, indicating a spatial inhomogeneity of the radiodensity estimates given by CBCT [18]. The correction procedure proposed in the present paper has the potential to mitigate this inhomogeneity.

Nackaerts *et al*. [15] observed that multislice CT gave constant HU values for all voxels of a homogeneous QCT-Bone Mineral phantom. In contrast, CBCT units gave inhomogeneous intensity profiles, which were roughly symmetric with respect to the symmetry axis of the FOV. Moreover, the intensity profiles were different for different types of scanners. Their observations are in agreement with our study: the CBCT intensity profiles recorded in the present study were symmetric with respect to the symmetry axis of the cylindrical FOV, and the spatial variability depicted in Figs. 2 and 3 was similar to two of the five types of scanners used in ref. [15]. Hence, the mathematical approach developed in this paper might be valid also for other types of CBCT scanners.

An important next step along the line of research presented here will aim at finding model parameters needed for clinically relevant corrections of CBCT voxel values. In Fig. 5, a precise correction would have rendered empty circles centered on stars (CT data for bone meal) and empty diamonds centered on + signs (CT data for $CaCl_2$). In such an ideal case, a CBCT measurement followed by the mathematical procedure proposed in this work would have given the radiodensity of each voxel with an accuracy that can only be achieved by a CT investigation, at higher costs and higher radiation exposure. Note that, in Fig. 6, even though the model parameters were inferred from the nonlinear least square fits of data recorded in the homogeneous part of the phantom (with *CT* numbers of about 100 HU), the corrected *CBCT* values closely follow CT numbers even in regions of high-radiodensity material (with *CT* numbers of about 528 HU). Hence, the model parameter estimation can be done, in principle, using phantoms that differ in composition from the hard tissues of the maxillofacial region. Inappropriate

parameters, however, make the correction procedure ineffective. For example, model parameters taken as the mean values of parameters inferred from measurements of granular $CaCl_2$ and bone meal samples, have led to a rough correction of *CBCT* voxel values in Fig. 6 (compare the plots represented by empty pentagons, solid disks, and stars).

CONCLUSION

This paper presented a mathematical procedure for improving bone quality assessment by CBCT. Relying on a mathematical relationship between *CT* numbers and *CBCT* voxel values, a correction formula has been proposed for HU values furnished by CBCT measurements. The corrected *CBCT* voxel values were in good agreement with *CT* numbers recorded by a fan-beam CT scanner.

For such a procedure to be successful in a clinical setting, one needs (i) to prove that the theoretical fit function (Eq. (1)) precisely accounts for the position dependence of *CBCT* voxel values, and (ii) find model parameters for oral hard tissues. Further research will be needed to validate the proposed correction procedure for several types of *CBCT* units.

Acknowledgements. We thank Dr. M. Leretter for insightful discussions on bone quality assessments using CBCT. This study was funded in part by the European Social Fund, Human Resources Development Operational Programme 2007–2013, Project no. POSDRU/159/1.5/136893.

REFERENCES

1. AZEREDO, F., L.M. DE MENEZES, R. ENCISO, A. WEISSHEIMER, R.B. DE OLIVEIRA, Computed gray levels in multislice and cone-beam computed tomography, *American Journal of Orthodontics and Dentofacial Orthopedics*, 2013, **144**, 147–155.
2. CARRAFIELLO, G., M. DIZONNO, V. COLLI, S. STROCCHI, S. POZZI TAUBERT, A. LEONARDI, *et al*., Comparative study of jaws with multislice computed tomography and cone-beam computed tomography, *Radiol. Med.*, 2010, **115**, 600–611.
3. CASSETTA, M., L.V. STEFANELLI, A. PACIFICI, L. PACIFICI, E. BARBATO, How accurate is CBCT in measuring bone density? A comparative CBCT-CT *in vitro* study. *Clinical Implant Dentistry and Related Research*, 2014, **16**, 471–478.
4. DAVID, O.T., M. LERETTER, A. NEAGU, The quality of trabecular bone assessed using cone-beam computed tomography, *Romanian J. Biophys.*, 2014, **24**, 227–241.
5. DE OLIVEIRA, R.C.G., C.R. LELES, L.M. NORMANHA, C. LINDH, R.F. RIBEIRO-ROTTA, Assessments of trabecular bone density at implant sites on CT images, *Oral Surgery Oral Medicine Oral Pathology Oral Radiology and Endodontology*, 2008, **105**, 231–238.
6. DE VOS, W., J. CASSELMAN, G.R.J. SWENNEN, Cone-beam computerized tomography (CBCT) imaging of the oral and maxillofacial region: A systematic review of the literature, *International Journal of Oral and Maxillofacial Surgery*, 2009, **38**, 609–625.

7. EMAM, H.A., M.R. STEVENS, Concepts in Bone Reconstruction for Implant Rehabilitation, in: M. Hosein, K. Motamedi (eds), *A Textbook of Advanced Oral and Maxillofacial Surgery*, InTech, Rijeka, 2013, Ch. 23, pp. 617–640.
8. FUH, L.J., H.L. HUANG, C.S. CHEN, K.L. FU, Y.W. SHEN, M.G. TU, W.C. SHEN, J.T. HSU, Variations in bone density at dental implant sites in different regions of the jaw bone, *Journal of Oral Rehabilitation*, 2010, **37**, 346–351.
9. GULSAHI A, Bone quality assessment for dental implants. In: I. Turkyilmaz (ed.), *Implant Dentistry – The Most Promising Discipline of Dentistry*, InTech, Rijeka, 2011, Ch. 20, pp. 437–452.
10. HAO, Y., W. ZHAO, Y. WANG, J. YU, D. ZOU, Assessments of jaw bone density at implant sites using 3D cone-beam computed tomography, *Eur. Rev. Med. Pharmacol. Sci.*, 2014, **18**, 1398–1403.
11. HIASA, K., Y. ABE, Y. OKAZAKI, K. NOGAMI, W. MIZUMACHI, Y. AKAGAWA, Preoperative computed tomography-derived bone densities in Hounsfield units at implant sites acquired primary stability. *ISRN Dentistry*, 2011, 678729.
12. MIRACLE, A.C., S.K. MUKHERJI, Cone beam CT of the head and neck, Part 1: Physical principles, *American Journal of Neuroradiology*, 2009, **30**, 1088–1095.
13. MISCH, C.E., Density of bone: effect on treatment plans, surgical approach, healing, and progressive bone loading. *The International Journal of Oral Implantology*: *Implantologist*, 1990, **6**, 23–31.
14. MISCH, C.E., *Contemporary Implant Dentistry*, Third Edition, Mosby Inc., St. Louis, 2008.
15. NACKAERTS, O., F. MAES, H. YAN, P. COUTO SOUZA, R. PAUWELS, R. JACOBS, Analysis of intensity variability in multislice and cone beam computed tomography. *Clinical Oral Implants Research*, 2011, **22**, 873–879.
16. NAITOH, M., A. HIRUKAWA, A. KATSUMATA, E. ARIJI, Evaluation of voxel values in mandibular cancellous bone: relationship between cone-beam computed tomography and multislice helical computed tomography, *Clinical Oral Implants Research*, 2009, **20**, 503–506.
17. NORTON, M. R., C. GAMBLE, Bone classification: an objective scale of bone density using the computerized tomography scan, *Clinical Oral Implants Research*, 2001, **12**, 79–84.
18. OLIVEIRA, M.L., G.M. TOSONI, D.H. LINDSEY, K. MENDOZA, S. TETRADIS, S.M. MALLYA, Influence of anatomical location on CT numbers in cone beam computed tomography, *Oral Surgery Oral Medicine Oral Pathology Oral Radiology and Endodontology*, 2013, **115**, 558–564.
19. PAUWELS, R., O. NACKAERTS, N. BELLAICHE, H. STAMATAKIS, K. TSIKLAKIS, A. WALKER, H. BOSMANS, R. BOGAERTS, R. JACOBS, K. HORNER, Variability of dental cone beam CT grey values for density estimations, *The British Journal of Radiology*, 2013, **86**, 20120135.
20. PAUWELS, R., R. JACOBS, S.R. SINGER, M. MUPPARAPU, CBCT-based bone quality assessment: are Hounsfield units applicable?, *Dento-maxillofacial Radiology*, 2015, **44**, 20140238.
21. SCARFE, W.C., A.G. FARMAN, P. SUKOVIC, Clinical applications of cone-beam computed tomography in dental practice, *Journal of the Canadian Dental Association*, 2006, **72**, 75–80.
22. SHAPURIAN, T., P.D. DAMOULIS, G.M. REISER, T.J. GRIFFIN, W.M. RAND, Quantitative evaluation of bone density using the Hounsfield index. *The International Journal of Oral & Maxillofacial Implants*, 2006, **21**, 290–297.
23. TURKYILMAZ, I., T.F. TOZUM, C. TUMER, Bone density assessments of oral implant sites using computerized tomography, *Journal of Oral Rehabilitation*, 2007, **34**, 267–272.